Article

Filopodia are a structural substrate for silent synapses in adult neocortex

https://doi.org/10.1038/s41586-022-05483-6

Received: 15 July 2021

Accepted: 25 October 2022

Published online: 30 November 2022

Check for updates

Dimitra Vardalaki[1,2], Kwanghun Chung[2,3,4,5,6] & Mark T. Harnett[1,2]✉

Newly generated excitatory synapses in the mammalian cortex lack sufficient AMPA-type glutamate receptors to mediate neurotransmission, resulting in functionally silent synapses that require activity-dependent plasticity to mature. Silent synapses are abundant in early development, during which they mediate circuit formation and refinement, but they are thought to be scarce in adulthood[1]. However, adults retain a capacity for neural plasticity and flexible learning that suggests that the formation of new connections is still prevalent. Here we used super-resolution protein imaging to visualize synaptic proteins at 2,234 synapses from layer 5 pyramidal neurons in the primary visual cortex of adult mice. Unexpectedly, about 25% of these synapses lack AMPA receptors. These putative silent synapses were located at the tips of thin dendritic protrusions, known as filopodia, which were more abundant by an order of magnitude than previously believed (comprising about 30% of all dendritic protrusions). Physiological experiments revealed that filopodia do indeed lack AMPA-receptor-mediated transmission, but they exhibit NMDA-receptor-mediated synaptic transmission. We further showed that functionally silent synapses on filopodia can be unsilenced through Hebbian plasticity, recruiting new active connections into a neuron's input matrix. These results challenge the model that functional connectivity is largely fixed in the adult cortex and demonstrate a new mechanism for flexible control of synaptic wiring that expands the learning capabilities of the mature brain.

Synaptic plasticity is implemented by the strengthening or weakening of neural connections as well as the formation of wholly new synapses or elimination of existing ones[2–5]. In the adult mammalian brain, plasticity is thought to manifest mainly through scalar changes in the synaptic strength of existing connections[6,7]. Although adult humans and other mammals exhibit powerful abilities to store and use new information, artificial neural networks with scalar synapses have not been able to match this level of performance[8,9]. Current models of adult plasticity may therefore be missing key biological principles and/or mechanisms. Silent synapses are prevalent in developing cortex, where they facilitate a highly flexible connectivity matrix[1,10,11]. Previous experimental investigations indicate that silent synapses are largely absent in adult cortex[1,12–14], but thus far, methods used to identify and evaluate silent synapses have been indirect. We reasoned that silent synapses could still be prevalent in mature brains, where they contribute to neural plasticity and learning.

To test this hypothesis, we carried out epitope-preserving magnified analysis of the proteome (eMAP)[15] to acquire super-resolution images of dendritic protrusions along with their synaptic AMPA (α-amino-3-hydroxy-5-methyl-4-isoxazole propionic acid) and NMDA (*N*-methyl-D-aspartate) receptor protein content in layer 5 (L5) pyramidal neurons from the primary visual cortex (V1) of adult mice. Brains were collected from four adult Thy1-GFP-M+ mice, which feature sparsely labelled cortical pyramidal neurons, mostly from L5 (Fig. 1a). We sampled synapses across the full cortical thickness of V1, randomly selecting in-plane dendritic segments from L5 pyramidal neurons for imaging (Fig. 1b,c). Within each approximately 20-µm-long dendritic segment, we annotated all protrusions. A total of 123 dendritic segments were imaged for a total of 2,234 dendritic protrusions in L5 pyramidal neurons. Unexpectedly, we found that filopodia, classically defined as protrusions lacking distinct heads (Fig. 1d,e and Extended Data Fig. 1), accounted for about 30% of the total number of dendritic protrusions imaged (Fig. 1f,g). This corresponds to an order of magnitude higher prevalence in adults than previously reported[16–19]. The high percentage of filopodia in adult L5 neurons is not a unique property of these cells, as we observed a similar percentage of filopodia in L2/3 neurons expressing virally transduced GFP (Fig. 1g and Extended Data Fig. 2).

We next evaluated whether these filopodia possessed synaptic receptors necessary for neurotransmission. We used antibodies against the presynaptic protein bassoon (which is involved in vesicle clustering) to visualize presynaptic compartments located adjacent to our GFP-expressing postsynaptic structures of interest[20]. Almost all spines (99.14%) and most filopodia (85.75%) exhibited a bassoon-defined presynaptic partner (Extended Data Fig. 3). Antibodies against GluA1 (also known as GRIA1) and GluN1 (GRIN1) were used to label AMPA receptors (AMPARs) and NMDA receptors (NMDARs), respectively. As expected,

[1]McGovern Institute for Brain Research, MIT, Cambridge, MA, USA. [2]Department of Brain & Cognitive Sciences, MIT, Cambridge, MA, USA. [3]Picower Institute for Learning and Memory, MIT, Cambridge, MA, USA. [4]Institute for Medical Engineering and Science, MIT, Cambridge, MA, USA. [5]Department of Chemical Engineering, MIT, Cambridge, MA, USA. [6]Broad Institute of Harvard University and MIT, Cambridge, MA, USA. ✉e-mail: harnett@mit.edu

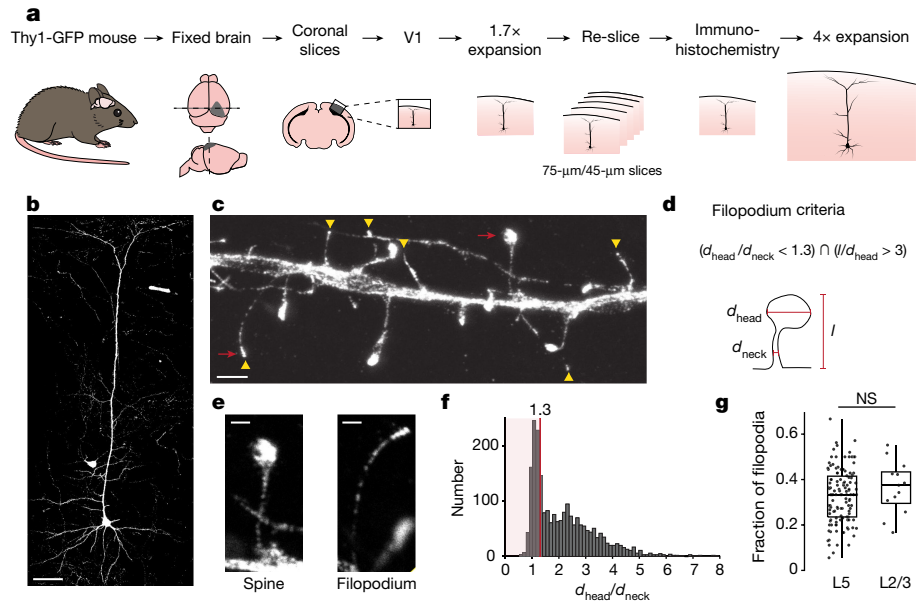

Fig. 1 | Filopodia account for a large fraction of dendritic protrusions in L5 and L2/3 pyramidal neurons of adult mouse primary visual cortex. **a**, A schematic of experimental tissue processing for expansion-based super-resolution imaging. **b**, An example confocal image of a Thy1-GFP-M+ L5 pyramidal neuron after 4× expansion of an originally 45-µm-thick slice. Scale bar, 200 µm (expanded)/50 µm (original). **c**, An example confocal image of an L5 pyramidal neuron dendritic segment after 4× expansion. The yellow arrowheads indicate filopodia. The red arrows indicate example spine and filopodium shown in **e**. Scale bar, 5 µm (expanded)/1.25 µm (original). **d**, An illustration of criteria to classify dendritic protrusions as spines or filopodia. **e**, A magnified image of a spine and a filopodium from **c** (red arrows). Scale bars, 2 µm (expanded)/0.5 µm (original). **f**, A histogram of d_{head}/d_{neck} (head/neck diameter ratios) across all dendritic protrusions ($n = 2{,}234$). The shaded area indicates $d_{head}/d_{neck} < 1.3$, one of the criteria used to classify protrusions as filopodia (see also Extended Data Fig. 1). **g**, The fraction of dendritic protrusions classified as filopodia (L5: $n = 2{,}234$ dendritic protrusions from 123 dendritic branches from 4 mice; L2/3: $n = 442$ dendritic protrusions from 13 dendritic branches from 3 mice). The box plot represents the median and the interquartile range (IQR) with whiskers extending to the most extreme points not considered outliers. $P = 0.33$ (NS, not significant; Kruskal–Wallis test).

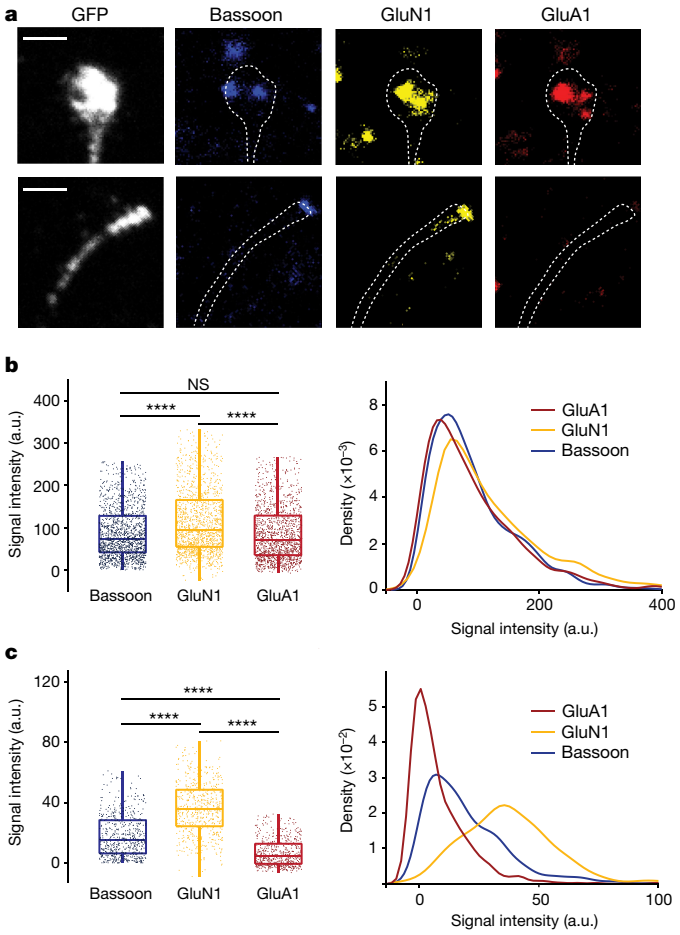

dendritic spines contained both AMPARs and NMDARs (Fig. 2a,b and Extended Data Fig. 4); the AMPAR signal increased as a function of spine head size, consistent with the findings of previous studies[21–23] (Extended Data Fig. 5). Filopodia, however, lacked AMPAR signals but exhibited robust NMDAR signals (Fig. 2a,c and Extended Data Figs. 2 and 4). Thus, using super-resolution protein imaging, filopodia appear as GluA1-immunonegative, GluN1-immunopositive protrusions that contact bassoon-immunopositive presynaptic membranes.

These results indicate that filopodia could contain synapses that are electrically silent at resting membrane potential, owing to voltage-dependent block of NMDARs by Mg^{2+}. Silent synapses have classically been defined as a mismatch between the number of responsive synapses at resting membrane potential and the number of responsive synapses at depolarized membrane potential[10,24,25]. Such synapses contain NMDARs but no or very few AMPARs. eMAP enables exceptional preservation of antigenicity; however, as with any other

Fig. 2 | Filopodia exhibit AMPAR-immunonegative and NMDAR-immunopositive synapses. **a**, Example four-channel images of a spine (top) versus a filopodium (bottom), from Fig. 1. From left to right: image of the cell-filling GFP stained with Alexa Fluor 488, presynaptic protein bassoon stained with Alexa Fluor 405 (blue), NMDAR subunit GluN1 stained with Alexa Fluor 555 (yellow) and AMPAR subunit GluA1 stained with Alexa Fluor 647 (red). Scale bars, 2 µm (expanded)/0.5 µm (original). **b**, A box plot (left) and kernel density estimate (right) of signal intensity in bassoon (blue), NMDAR (yellow) and AMPAR (red) channels for spines ($n = 1{,}505$). The box plot represents the median and IQR with whiskers extending to the most extreme points not considered outliers. The signal in each channel is shown for all dendritic protrusions, each represented by one dot. a.u., arbitrary units. NS, $P = 0.1331$; $^{****}P = 2 \times 10^{-21}$ for bassoon versus GluN1, and $^{****}P = 1 \times 10^{-25}$ for NMDA versus GluA1 (Kruskal–Wallis test). **c**, As in **b**, but for filopodia ($n = 614$). $^{****}P = 8 \times 10^{-66}$ for bassoon versus GluN1, $^{***}P = 4 \times 10^{-140}$ for NMDA versus GluA1, and $^{****}P = 1 \times 10^{-49}$ for bassoon versus GluA1 (Kruskal–Wallis test).

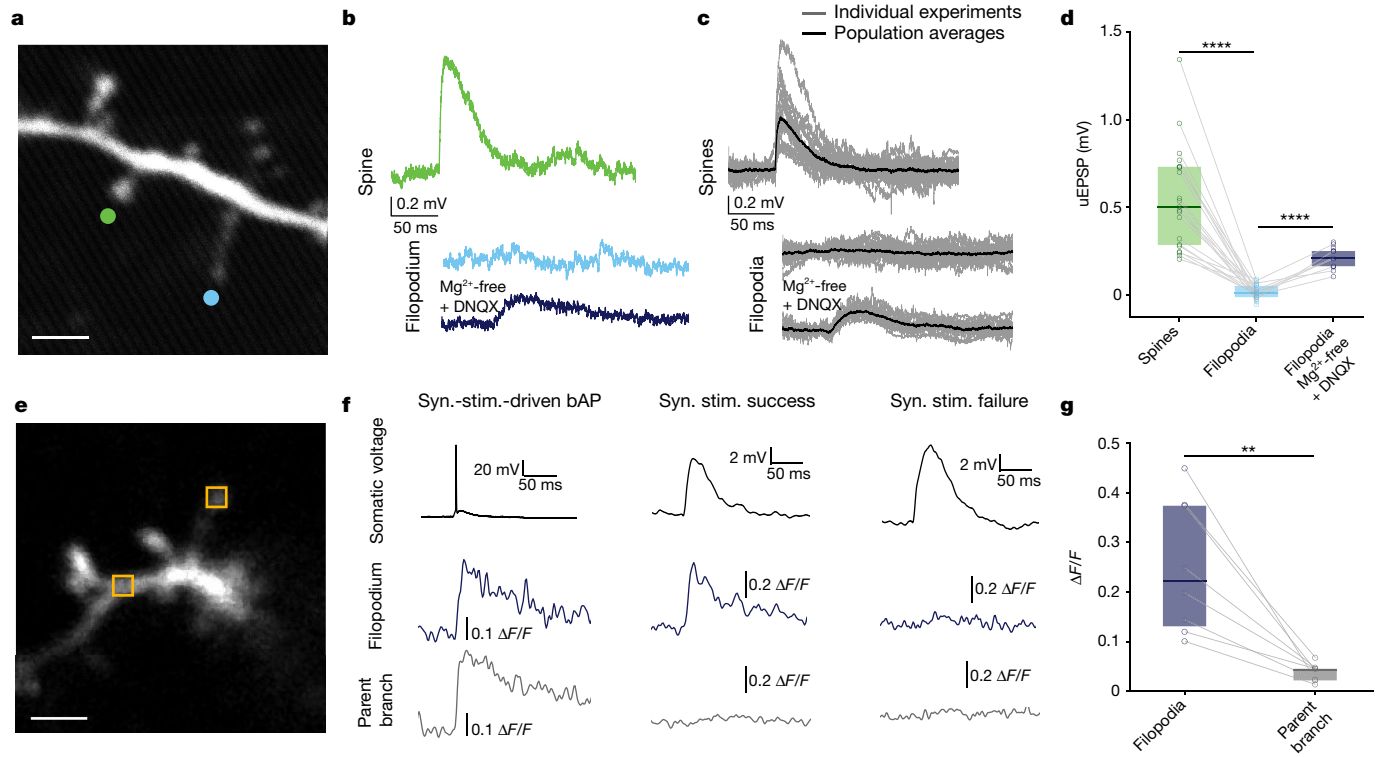

Fig. 3 | Filopodia lack AMPAR- but exhibit NMDAR-mediated transmission and release-competent presynaptic partners. a, An example two-photon image of a basal dendritic branch from an L5 V1 pyramidal neuron filled with Alexa Fluor 488. Two-photon glutamate uncaging locations are indicated at a test spine (green circle) and a filopodium (light blue circle). Scale bar, 2 µm. **b**, Voltage traces recorded at the soma in response to two-photon glutamate uncaging at the spine shown in **a** (top),the filopodium shown in **a** (middle) and the same filopodium in Mg^{2+}-free aCSF with AMPARs blocked (20 µM DNQX; bottom). **c**, Voltage traces recorded in somas in response to two-photon glutamate uncaging at spines (top, $n = 21$ spines from 19 slices and 15 mice), filopodia (middle, $n = 22$ filopodia from 20 slices and 16 mice) and filopodia in Mg^{2+}-free aCSF with AMPARs blocked (bottom, $n = 15$ filopodia from 15 slices and 9 mice). Individual spine and filopodium traces are shown in grey; population averages are shown in black. **d**, A population comparison of peak amplitudes of uncaging-evoked responses from **c**. $^{****}P = 1 \times 10^{-8}$ for spines versus filopodia, and $^{****}P = 3 \times 10^{-7}$ for filopodia in control versus Mg^{2+}-free (+DNQX) aCSF (Kruskal–Wallis test). The box plot represents the median and IQR. uEPSP, uncaging-evoked EPSP. **e**, An example two-photon image of a dendritic branch from an L5 V1 pyramidal neuron filled with Alexa Fluor 594 and Fluo-4. Changes in intracellular Ca^{2+} were measured via the Fluo-4 signal at the filopodium and the parent dendrite (yellow squares) in response to focal extracellular synaptic stimulation. Scale bar, 2 µm **f**, Somatic voltage recording (top) and the corresponding changes in local Ca^{2+} ($\Delta F/F$) at the tip of the filopodium shown in **e** (middle) and the parent dendritic branch shown in **e** (bottom) in response to focal extracellular synaptic (syn.) stimulation (stim.) in Mg^{2+}-free aCSF with AMPARs blocked. bAP, backpropagating action potential. **g**, Population analysis of the peak local Ca^{2+} signal in filopodia and their respective parent branches for synaptic stimulation successes ($n = 8$ filopodia from 5 slices and 3 mice). $^{**}P = 0.0078$ (two-sided Wilcoxon signed-rank test). The box plot represents the median and IQR.

immunohistochemical technique, low levels of protein expression may be difficult to detect. By combining whole-cell patch-clamp electrophysiology with two-photon glutamate uncaging and imaging, we directly tested whether filopodia represent functionally silent synapses in brain slices of adult mouse primary visual cortex. We filled L5 pyramidal neurons with a structural dye (Alexa Fluor 488) to target two-photon glutamate uncaging onto identified postsynaptic structures. We could observe only a subset of filopodia under optimized two-photon imaging owing to the resolution limit and the optical aberration associated with other nearby brightly labelled structures such as large spines and parent dendrites. We calibrated the uncaging laser power using spines near (<10 µm) targeted filopodia, such that spine uncaging elicited large (0.2–1.2 mV) somatic excitatory postsynaptic potentials (EPSPs) (Fig. 3a,b and Extended Data Fig. 6). All spines tested (21 out of 21) exhibited synaptic responses to glutamate uncaging. By contrast, none of the filopodia (22 out of 22) responded to glutamate uncaging (Fig. 3b–d). The lack of somatic response could be due to lack of AMPARs, or to filtering across the long, potentially high-resistance filopodium neck. To disambiguate these possibilities, we used Mg^{2+}-free artificial cerebrospinal fluid (aCSF) to relieve the voltage dependence of NMDARs while also blocking AMPARs (with 20 µM 6,7-dinitroquinoxaline-2,3-dione (DNQX)). Under these conditions, we observed NMDAR-mediated EPSPs in response to glutamate uncaging at filopodia (Fig. 3b–d). These results indicate that neck resistance filtering is not responsible for the lack of AMPA-mediated responses at filopodia. Instead, our physiological data demonstrate that filopodia lack AMPAR-mediated transmission but do exhibit NMDAR-mediated transmission, consistent with our protein imaging results.

Most filopodia exhibited bassoon-defined presynaptic partners, but it is not clear from our uncaging experiments whether filopodium-associated presynaptic structures are vesicle release competent. To test this, we looked for synaptically evoked local Ca^{2+} transients in filopodia in response to electrical microstimulation of nearby axons[26,27]. We filled L5 pyramidal neurons with a structural dye (Alexa Fluor 594) and a calcium indicator (Fluo-4) and placed a bipolar theta glass microelectrode about 10 µm from a dendritic branch with an identified filopodium. Microstimulation was conducted in Mg^{2+}-free aCSF with AMPARs blocked (20 µM DNQX). We assessed synaptic transmission by measuring local Ca^{2+} transients (through Fluo-4) in filopodia (Fig. 3e,f and Extended Data Fig. 7). We observed large local Ca^{2+} signals in response to microstimulation in the tip of filopodia that were not detectable in the parent dendrite, indicating that their associated presynaptic structures are indeed release competent. We could distinguish successful transmitter release from failure of release, and these

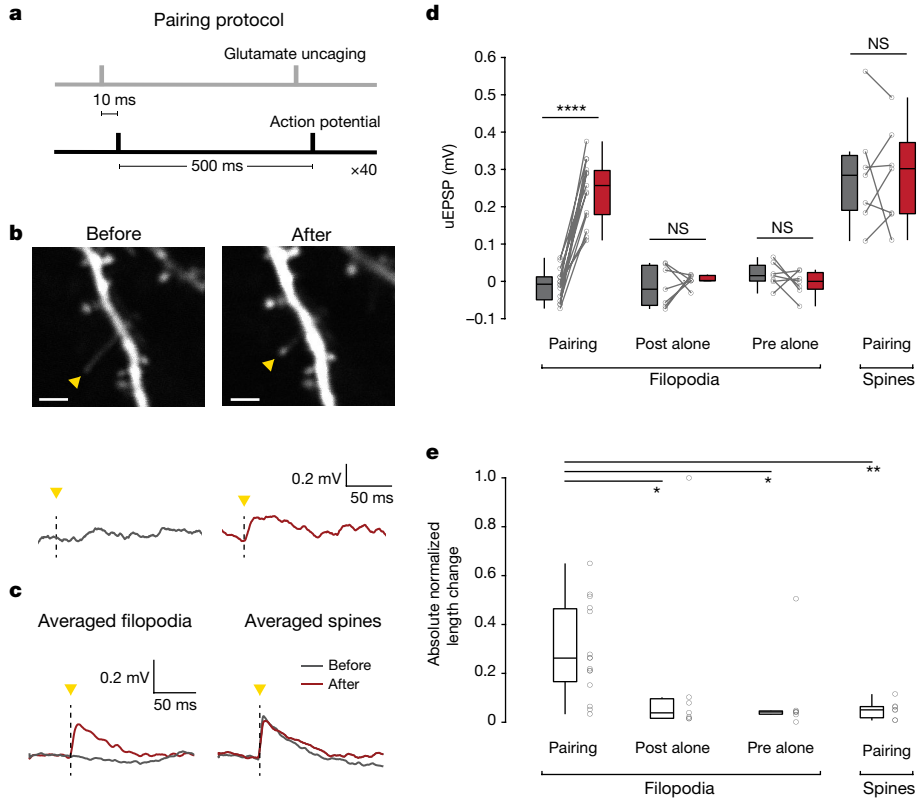

Fig. 4 | Silent synapses at filopodia can be unsilenced by Hebbian pairing. **a**, Schematic of the induction pairing protocol. **b**, Representative images (top) and somatic voltage traces (bottom) in response to two-photon glutamate uncaging test pulses at a filopodium before (left) and after (right) induction. Yellow arrowheads indicate two-photon glutamate uncaging location (top) and timing (bottom). Scale bars, 2 µm. **c**, Population-averaged somatic voltage traces evoked by two-photon glutamate uncaging at filopodia (left, $n = 15$ filopodia from 13 slices and 10 mice) and at spines (right, $n = 7$ spines from 7 slices and 4 mice) before (grey) and after (red) induction. **d**, Peak somatic uncaging-evoked EPSP amplitude before (grey) and after (red) induction in filopodia and spines. Three different induction protocols were tested in filopodia: pairing protocol ($n = 15$ filopodia from 13 slices and 10 mice); somatic action potentials without any caged glutamate present (post alone; $n = 7$ filopodia from 7 slices and 6 mice); pairing protocol without somatic action potential (pre alone; $n = 7$ filopodia from 7 slices and 6 mice); $^{****}P = 6 \times 10^{-5}$; NS, $P = 0.46$ for post alone, 0.29 for pre alone, and 0.81 for spines. Two-sided Wilcoxon signed-rank test. The box plot represents the median and the IQR with whiskers extending to the most extreme points not considered outliers. **e**, Absolute normalized protrusion length change after induction in the filopodia and spines from **d** (also see Extended Data Fig. 8). The box plot represents the median and the IQR with whiskers extending to the most extreme points not considered outliers; $^{*}P = 0.0316$ for pairing versus post alone, and $^{*}P = 0.0101$ for pairing versus pre alone; $^{**}P = 0.0027$; Kruskal–Wallis test.

events were clearly distinct from widespread electrical events such as backpropagating action potentials (Fig. 3e,g). Combined with our glutamate uncaging and super-resolution protein imaging experiments, these results demonstrate that filopodia are a structural substrate for silent synapses in the adult brain.

The activity-dependent conversion of silent to functional synapses plays a key role in developmental plasticity[2,28,29]. However, the contribution of silent synapses to adult cortical plasticity has not been explored owing to the previous model of low silent synapse prevalence in adult brain. We therefore asked whether adult silent synapses at filopodia can be converted into active (that is, not silent) synapses. Several studies have previously provided evidence for unsilencing silent synapses at the population level in the developing brain[10,25,30,31]. Exploiting our ability to morphologically identify silent synapses, we tested whether they could be 'unsilenced' at the individual level in the adult brain. We used a spike-timing-dependent plasticity protocol in which presynaptic activity was mimicked by glutamate uncaging at filopodia and closely followed (10 ms later) by current injection in the soma of the postsynaptic neuron to produce a single action potential (Fig. 4a). After induction of the plasticity protocol, the length of filopodia changed (9 out of 15 decreased by 36 ± 6%, and 6 out of 15 increased by 18 ± 7%; Extended Data Fig. 8). Furthermore, induction resulted in the appearance of AMPAR-mediated synaptic responses at filopodia on the timescale of minutes (Fig. 4b–d). The structural and functional changes in filopodia were observed only when presynaptic and postsynaptic activity was paired (Fig 4d,e). Unexpectedly, this protocol did not induce either structural or functional plasticity at conventional spiny synapses (Fig. 4c–e and Extended Data Fig. 9). This is in contrast to the findings of previous reports, in which the same protocol plasticized spines in the juvenile brain[32]. Plasticity was not induced at spines even when we more than doubled the number of EPSP–action potential pairings (Extended Data Fig. 9). Thus, a spike-timing-dependent plasticity protocol is insufficient to induce synaptic plasticity in spines of adult animals but is sufficient to unsilence silent synapses, demonstrating a hierarchy of plasticity thresholds for different synaptic classes in the adult mammalian cortex.

The super-resolution imaging technique we applied here allowed us to resolve structures well below the diffraction limit[15,33]. Although eMAP retains original micro-architecture without distortion[15], to compare our approach with the existent literature on synapse morphology in juveniles, we carried out eMAP in three Thy1-GFP-M+ mice at postnatal day 13 (Extended Data Fig. 10). In accordance with previous reports[16], our experiments revealed a high percentage of shaft synapses at postnatal day 13 (Extended Data Fig. 10). Furthermore, our morphological measurements of dendritic protrusions in adults are consistent with previous electron microscopy measurements[34] (Extended Data Fig. 1).

Our eMAP experiments revealed small postsynaptic structural details, including filopodia, that are usually hidden in the haze of fluorescence around dendrites and large spines in conventional light microscopy. The combination of physical enlargement of the tissue, single-cell morphological contrast and optical clearing allowed for nanoscopic investigation of synaptic structures. In addition to the unexpectedly high number of filopodia we observed (about 30% of dendritic protrusions in mouse V1 L5 and L2/3 pyramidal neurons), we further discovered a high number of functionally silent synapses in the adult cortex. Silent synapses have classically been studied with indirect electrophysiology techniques in the developing brain[30,35]. With the exception of the nucleus accumbens[36], this approach has failed to identify silent synapses in the adult brain. Previous immunogold-labelling electron microscopy studies have provided evidence that synapses lacking AMPARs may be present in adult brain[21,22,37], particularly at smaller dendritic protrusions. Yet the limited numbers of these studies, the small sizes of the samples and concerns regarding immunogold antibody affinity have made it challenging to infer the structure–function relationship and prevalence of silent synapses.

We present data directly linking dendritic filopodia to silent synapses, showing that they represent a substantial and previously unknown reservoir for adult cortical plasticity. Furthermore, our experiments demonstrate that silent synapses have a different threshold for plasticity compared with that of non-silent synapses, which is consistent with theoretical models of flexible and robust memory[9,38–40]. Specifically, memory formation requires a balance between flexibility and stability: flexibility establishes memory acquisition and stability ensures memory retention. It is unknown whether the processes governing stability versus flexibility operate at the synaptic level. Dendritic protrusions, in the form of filopodia and spines, span a continuum of morphologies[19,34], and it remains to be tested whether this continuum of morphologies reflects synaptic states, along which both synaptic strength and plasticity thresholds vary. Our data are consistent with a model in which mature synapses at spines stably store acquired information, and silent synapses at filopodia mediate the rapid acquisition of new information.

Online content

Any methods, additional references, Nature Portfolio reporting summaries, source data, extended data, supplementary information, acknowledgements, peer review information; details of author contributions and competing interests; and statements of data and code availability are available at https://doi.org/10.1038/s41586-022-05483-6.

1. Hanse, E., Seth, H. & Riebe, I. AMPA-silent synapses in brain development and pathology. *Nat. Rev. Neurosci.* **14**, 839–850 (2013).
2. Katz, L. C. & Shatz, L. C. Synaptic activity and the construction of cortical circuits. *Science* **274**, 1133–1138 (1996).
3. Magee, J. C. & Grienberger, C. Synaptic plasticity forms and functions. *Annu. Rev. Neurosci.* **43**, 95–117 (2020).
4. Trachtenberg, J. T. et al. Long-term in vivo imaging of experience-dependent synaptic plasticity in adult cortex. *Nature* **420**, 788–794 (2002).
5. Knott, G. W., Holtmaat, A., Wilbrecht, L., Welker, E. & Svoboda, K. Spine growth precedes synapse formation in the adult neocortex in vivo. *Nat. Neurosci.* **9**, 1117–1124 (2006).
6. Grutzendler, J., Kasthuri, N. & Gan, W. B. Long-term dendritic spine stability in the adult cortex. *Nature* **420**, 812–816 (2002).
7. Holtmaat, A. J. G. D. et al. Transient and persistent dendritic spines in the neocortex in vivo. *Neuron* **45**, 279–291 (2005).
8. Fusi, S. & Abbott, L. F. Limits on the memory storage capacity of bounded synapses. *Nat. Neurosci.* **10**, 485–493 (2007).
9. Poirazi, P. & Mel, B. W. Impact of active dendrites and structural plasticity on the memory capacity of neural tissue. *Neuron* **29**, 779–796 (2001).
10. Durand, G. M., Kovalchuk, Y. & Konnerth, A. Long-term potentiation and functional synapse induction in developing hippocampus. *Nature* **381**, 71–75 (1996).
11. Huang, X. et al. Progressive maturation of silent synapses governs the duration of a critical period. *Proc. Natl Acad. Sci. USA* **112**, E3131–E3140 (2015).
12. Busetto, G., Higley, M. J. & Sabatini, B. L. Developmental presence and disappearance of postsynaptically silent synapses on dendritic spines of rat layer 2/3 pyramidal neurons. *J. Physiol.* **586**, 1519–1527 (2008).
13. Isaac, J. T. R., Crair, M. C., Nicoll, R. A. & Malenka, R. C. Silent synapses during development of thalamocortical inputs. *Neuron* **18**, 269–280 (1997).
14. Anastasiades, P. G. & Butt, S. J. B. A role for silent synapses in the development of the pathway from layer 2/3 to 5 pyramidal cells in the neocortex. *J. Neurosci.* **32**, 13085–13099 (2012).
15. Park, J. et al. Epitope-preserving magnified analysis of proteome (eMAP). *Sci. Adv.* **7**, eabf6589–eabf6589 (2021).
16. Fiala, J. C., Feinberg, M., Popov, V. & Harris, K. M. Synaptogenesis via dendritic filopodia in developing hippocampal area CA1. *J. Neurosci.* **18**, 8900–8911 (1998).
17. Zuo, Y., Lin, A., Chang, P. & Gan, W. B. Development of long-term dendritic spine stability in diverse regions of cerebral cortex. *Neuron* **46**, 181–189 (2005).
18. Dunaevsky, A., Tashiro, A., Majewska, A., Mason, C. & Yuste, R. Developmental regulation of spine motility in the mammalian central nervous system. *Proc. Natl Acad. Sci. USA* **96**, 13438–13443 (1999).
19. Berry, K. P. & Nedivi, E. Spine dynamics: are they all the same? *Neuron* **96**, 43–55 (2017).
20. Gundelfinger, E. D., Reissner, C. & Garner, C. C. Role of Bassoon and Piccolo in assembly and molecular organization of the active zone. *Front. Synaptic Neurosci.* **7**, 19 (2016).
21. Nusser, Z. et al. Cell type and pathway dependence of synaptic AMPA receptor number and variability in the hippocampus. *Neuron* **21**, 545–559 (1998).
22. Kharazia, V. N. & Weinberg, R. J. Immunogold localization of AMPA and NMDA receptors in somatic sensory cortex of albino rat. *J. Comp. Neurol.* **412**, 292–302 (1999).
23. Holler, S., Köstinger, G., Martin, K. A. C., Schuhknecht, G. F. P. & Stratford, K. J. Structure and function of a neocortical synapse. *Nature* **591**, 111–116 (2021).
24. Liao, D., Scannevin, R. H. & Huganir, R. Activation of silent synapses by rapid activity-dependent synaptic recruitment of AMPA receptors. *J. Neurosci.* **21**, 6008–6017 (2001).
25. Isaac, J. T. R., Nicoll, R. A. & Malenka, R. C. Evidence for silent synapses: implications for the expression of LTP. *Neuron* **15**, 427–434 (1995).
26. Mainen, Z. F., Malinow, R. & Svoboda, K. Synaptic calcium transients in single spines indicate that NMDA receptors are not saturated. *Nature* **399**, 151–155 (1999).
27. Oertner, T. G., Sabatini, B. L., Nimchinsky, E. A. & Svoboda, K. Facilitation at single synapses probed with optical quantal analysis. *Nat. Neurosci.* **5**, 657–664 (2002).
28. Kerchner, G. A. & Nicoll, R. A. Silent synapses and the emergence of a postsynaptic mechanism for LTP. *Nat. Rev. Neurosci.* **9**, 813–825 (2008).
29. Lisman, J. E., Raghavachari, S. & Tsien, R. W. The sequence of events that underlie quantal transmission at central glutamatergic synapses. *Nat. Rev. Neurosci.* **8**, 597–609 (2007).
30. Liao, D., Hessler, N. A. & Malinow, R. Activation of postsynaptically silent synapses during pairing-induced LTP in CA1 region of hippocampal slice. *Nature* **375**, 400–404 (1995).
31. Zhu, J. J., Esteban, J. A., Hayashi, Y. & Malinow, R. Postnatal synaptic potentiation: delivery of GluR4-containing AMPA receptors by spontaneous activity. *Nat. Neurosci.* **3**, 1098–1106 (2000).
32. Tazerart, S., Mitchell, D. E., Miranda-Rottmann, S. & Araya, R. A spike-timing-dependent plasticity rule for dendritic spines. *Nat. Commun.* **11**, 4276 (2020).
33. Wassie, A. T., Zhao, Y. & Boyden, E. S. Expansion microscopy: principles and uses in biological research. *Nat. Methods* **16**, 33–41 (2019).
34. Ofer, N., Berger, D. R., Kasthuri, N., Lichtman, J. W. & Yuste, R. Ultrastructural analysis of dendritic spine necks reveals a continuum of spine morphologies. *Dev. Neurobiol.* **81**, 746–757 (2021).
35. Kullmann, D. M. Amplitude fluctuations of dual-component EPSCs in hippocampal pyramidal cells: implications for long-term potentiation. *Neuron* **12**, 1111–1120 (1994).
36. Wright, W. J. et al. Silent synapses dictate cocaine memory destabilization and reconsolidation. *Nat. Neurosci.* **23**, 32–46 (2020).
37. Takumi, Y., Ramírez-León, V., Laake, P., Rinvik, E. & Ottersen, O. P. Different modes of expression of AMPA and NMDA receptors in hippocampal synapses. *Nat. Neurosci.* **2**, 618–624 (1999).
38. Benna, M. K. & Fusi, S. Computational principles of synaptic memory consolidation. *Nat. Neurosci.* **19**, 1697–1706 (2016).
39. Fusi, S., Drew, P. J. & Abbott, L. F. Cascade models of synaptically stored memories. *Neuron* **45**, 599–611 (2005).
40. Aitchison, L. et al. Synaptic plasticity as Bayesian inference. *Nat. Neurosci.* **24**, 565–571 (2021).

Methods

Animals

All animal procedures were carried out in compliance with the National Institutes of Health and Massachusetts Institute of Technology Committee on Animal Care guidelines. The study protocol in the manuscript has been approved by the Massachusetts Institute of Technology Committee on Animal Care. We used C57BL/6 mice (Charles River Laboratories) for the electrophysiology experiments and viral injections, and Thy1-GFP-M mice (Jackson Laboratory, stock no. 007788) for L5 pyramidal neuron super-resolution experiments. Half of the mice used for the electrophysiology experiments were housed with 2–5 littermates in a large cage (19 × 10.5 × 6 in (48 × 27 × 15 cm)) with a running wheel and plastic shelter tubes. We did not observe any difference between the conventionally and the enriched housed mice. After virus injection, mice were individually housed for 2 weeks. Male and female mice were used in approximately equal numbers for all experiments at 8–10 weeks of age. Mice were kept on a 12-h light/dark cycle and had unrestricted access to food and water in a room at 20–22 °C and 35–45% humidity. Sample sizes are comparable to or larger than those for similar studies. No randomization was possible with the study design. Blinding was used in image analysis as detailed in the section below.

Magnified analysis of the proteome

Two male and two female Thy1-GFP-M mice were used for the adult L5 protein imaging dataset. One male and two female Thy1-GFP-M mice were used for the postnatal day 13 (P13) protein imaging dataset. We noted that 2 other Thy1-GFP-M mice at P13 exhibited no GFP-labelled L5 cortical pyramidal neurons in V1. The expression of GFP in the positive P13 mice was very sparse with only 1–2 L5 pyramidal neurons per hemisphere in V1. This is consistent with the developmental regulation of the expression of GFP in *Thy1* transgenic animals[7,41].

Two male C57BL6 mice and one female C57BL/6 mouse injected with a GFP-expressing virus were used for the L2/3 protein imaging dataset. These mice were 7 weeks-old at the time of viral injection. All surgeries were carried out under aseptic conditions and stereotaxic guidance. Mice were anaesthetized with isoflurane (2% induction, 0.75%–1.25% maintenance in 1 l min^{-1} oxygen) and secured in a stereotaxic apparatus. Body temperature was maintained with a feedback-controlled heating pad (DC Temperature 21 Control System, FHC). Slow-release buprenorphine (1 mg kg^{-1}) was pre-operatively injected subcutaneously. The scalp was cleaned with iodine solution and alcohol. After incision of the scalp, a small burr hole was made using a dental air drill. Mice were injected bilaterally in V1 (stereotactic coordinates: 2.9 mm lateral, 0.4 mm anterior to lambda) with undiluted pAAV1-hSyn-DIO-eGFP virus (Addgene catalogue no. 50457-AAV1) mixed in a 1:1 ratio with 1:10,000 diluted pENN.AAV.CamKII 0.4.Cre.SV40 virus (Addgene catalogue no. 105558-AAV9). Virus was delivered at a slow rate (maximum 50 nl min^{-1}) to prevent tissue damage through a small, bevelled injection pipette. Virus was injected at an initial depth of 350 µm below the pial surface and moving up 150 µm for a second injection, for a total of approximately 300 nl of injected virus across cortical L2/3. The low volume for these experiments was chosen to achieve optimal sparsity for observing pyramidal cell processes. After a 5-min rest, the pipette was slowly withdrawn, and the incision was sutured. Mice were given 2 weeks to recover and for virus expression before perfusion.

Mice were perfused intracardially with cold PBS followed by cold 4% PFA while under deep anaesthesia (5% isoflurane). Brains were removed and kept in the same fixative overnight at 4 °C, and then washed with PBS at 4 °C for 1 day. Coronal slices, 1.0 mm, of primary visual cortex were cut on a vibratome and kept in PBS at 4 °C until the day of processing. Slices were then incubated in the eMAP hydrogel monomer solution: 30% acrylamide (A9099, Millipore Sigma), 10% sodium acrylate (408220, Millipore Sigma), 0.1% bis-acrylamide (161-0142, Bio-Rad Laboratories) and 0.03% VA-044 (w/v) (Wako Chemicals) in PBS, at 4 °C for 8 to 12 h. The slices were subsequently mounted between glass slides and sealed in a 50-ml conical tube with nitrogen gas at positive pressure of 10–12 psi for embedding at 35 °C for 3 h. The excess gel around the slices was then removed. To reach a first expansion stage of 1.7×, the slices were then incubated in a solution of 0.02% sodium azide (w/v) in PBS at 37 °C. Slices were trimmed to contain only parts of primary visual cortex and further sectioned with a vibratome to 75 µm thickness (corresponding to approximately 45 µm thickness of the pre-expanded tissue). Slices containing good candidate cells—L5 pyramidal neurons whose apical trunk could be reconstructed at its full length in a single slice or at most two consecutive slices—were selected during live low-resolution confocal imaging sessions for further processing. These slices were trimmed to smallest possible samples of approximately 1.0 mm in both width and length. Then they were incubated in tissue clearing solution (6% SDS (w/v), 0.1 M phosphate buffer, 50 mM sodium sulfite, 0.02% sodium azide (w/v), pH 7.4) at 37 °C for 6 h, followed by incubation in preheated clearing solution at 95 °C for 10 min. Cleared samples were thoroughly washed with PBS + 0.1% Triton-X at 37 °C.

Primary antibody staining was carried out at 37 °C overnight with the following antibodies: anti-GFP (Life Technologies A10262), anti-NMDAR1 (SYSY 114011), anti-AMPAR1 (SYSY 182003), anti-bassoon (SYSY 141004) (typical dilution 1:20). For secondary staining, the following fluorescent antibodies were used: bassoon, anti-GP IgG-Alexa Fluor 405; GFP, anti-chicken IgY(H+L)-Alexa Fluor 488; NMDAR1, anti-mouse IgG-Alexa Fluor 555; and AMPAR1, anti-rabbit IgG-Alexa Fluor 647 (typical dilution 1:10). Final expansion was carried out just before imaging by putting the trimmed slices in 0.1 mM Tris in distilled water. Approximately 4× total linear expansion was achieved, and dendritic branches of candidate cells were imaged on a Leica TCS SP8 upright confocal DM6000 microscope equipped with a 63× 1.2 NA water immersion objective (300 µm working distance), hybrid detectors and a white light laser. Leica Application Suite X was used for image acquisition.

We imaged 123 segments from L5 neurons. Of these, 56 originated in basal, 45 in oblique, 20 in trunk and 2 in tuft dendrites. Each image contained a dendritic branch and its dendritic protrusions: spines and filopodia. Dendritic protrusions were analysed in the GFP channel using ImageJ software. We used a custom-written macro code that first applies a median blur (2 pixels) in the GFP image and then converts the tip of individual dendritic protrusions to binary masks by thresholding the resulting GFP image. The rest of the analysis was carried out using custom-written MATLAB code. Each channel (bassoon, GFP, NMDAR and AMPAR) was binarized using intensity thresholds (mean + 2 s.d. of the intensity values in each image). Only the protrusions that exhibited a bassoon-defined presynaptic partner (Extended Data Fig. 3) qualified as synapses, and were further analysed. The intensity signal in each of the four channels was finally calculated as the intensity difference of the mask containing the structure of interest and the background. The background intensity was calculated by using the same mask but at random x–y locations of the image to account for the effect of size in the measured intensity among dendritic protrusions. For experiments in L2/3 pyramidal neurons, the first 350 background draws from the total 400 (ranked with increasing intensity) were used to calculate the background. This adjustment was used to account for the very high synaptic density in L2/3. Long and thin dendritic protrusions without an enlarged head were classified as filopodia (head diameter/neck diameter < 1.3 and length/head diameter > 3). These definitions were based on previous reports[16,17,42]. Dendritic protrusions with an enlarged head were classified as spines. The head and neck diameters were measured perpendicular to the long axis of the neck at the widest point. All measurements were made blindly to the bassoon, AMPAR and NMDAR channels.

Acute cortical slice preparation

Coronal brain slices (300 µm) containing the primary visual cortex (V1) were prepared from 8- to 10-week-old C57BL/6 mice. Mice were deeply anaesthetized with isoflurane before decapitation. The brain was removed

and sliced with a vibratome (Leica) in ice-cold slicing solution containing 90 mM sucrose, 60 mM NaCl, 26.5 mM $NaHCO_3$, 2.75 mM KCl, 1.25 mM NaH_2PO_4, 1.1 mM $CaCl_2$, 5 mM $MgCl_2$, 9 mM glucose, 3 mM sodium pyruvate and 1 mM ascorbic acid, saturated with 95% O_2 and 5% CO_2. Slices were incubated in aCSF containing 120 mM NaCl, 3 mM KCl, 25 mM $NaHCO_3$, 1.25 mM NaH_2PO_4, 1.2 mM $CaCl_2$, 1.2 mM $MgCl_2$, 11 mM glucose, 3 mM sodium pyruvate and 1 mM ascorbic acid, saturated with 95% O_2 and 5% CO_2 at 35.5 °C for 25–30 min and then stored at room temperature. All recordings were carried out at 32–35 °C in aCSF. As indicated in the figure legends, Mg^{2+} was omitted from aCSF in some experiments. For focal synaptic stimulation experiments (Fig. 2), the aCSF contained 2 mM $CaCl_2$ and 0 nm $MgCl_2$.

Patch-clamp recording

An Olympus BX-61 microscope with infrared Dodt optics and a 60× water immersion lens (Olympus) was used to visualize cells. Patch-clamp recordings were carried out from morphologically and electrophysiologically identified L5b pyramidal cells in V1. Current-clamp recordings were carried out in bridge mode with a Dagan BVC-700 amplifier with the bridge fully balanced. Current and voltage signals were filtered at 10 kHz and digitized at 20 kHz. Patch pipettes were prepared with thin-wall glass (1.5 outer diameter; 1.1 inner diameter). Pipettes had resistances ranging from 3 to 7 MΩ, and the capacitance was fully neutralized before break in. Series resistances ranged from 6 to 25 MΩ. The intracellular solution contained: 134 mM potassium gluconate, 6 mM KCl, 10 mM HEPES buffer, 4 mM NaCl, 4 mM Mg_2ATP, 3 mM NaGTP and 14 mM phosphocreatine di (tris). Depending on the experiment, 0.1 mM Alexa Fluor 488 (Invitrogen) or 0.05 mM Alexa Fluor 594 (Invitrogen) and 0.2 mM Fluo-4 (Invitrogen) were added to the intracellular solution. Bruker Prairie View Software was used for the data acquisition.

Two-photon imaging and uncaging

A two-photon laser scanning system (Prairie Technologies Ultima) with dual galvanometers and two ultrafast pulsed lasers beams (Mai Tai DeepSee lasers) was used to simultaneously image and uncage glutamate. One path was used to image Alexa Fluor 488 at 920 nm. The other path was used to photolyse MNI-caged L-glutamate (Tocris) at 720 nm. Stock MNI solutions (50 mM) were freshly diluted in aCSF to 10 mM, and a Picospritzer (General Valve) was used to focally apply the MNI-caged L-glutamate through pressure ejection through a large glass pipette above the slice. Laser beam intensity was independently controlled with electro-optical modulators (model 350-50; Conoptics). Emitted light was collected by GaAsP photomultipliers. Uncaging dwell time was 0.2 ms. A passive 8× pulse splitter in the uncaging path was used to reduce photodamage[43,44]. Experiments were terminated if signs of photodamage were detected (increase in basal fluorescence, loss of transient signals and/or depolarization). Filopodia were identified by their long and thin morphology without an enlarged head (head/neck diameter < 1.3 and length/head diameter > 3). All uncaging experiments on filopodia were conducted with a neighbouring control spine. The laser power of the uncaging laser was adjusted to elicit somatic responses when neighbouring spines were targeted. Uncaging locations were manually positioned in close vicinity (<0.5 µm) from the tip of the spine or filopodium. The uncaging locations were manually readjusted if necessary between individual trials. Care was taken to ensure that the selected spines or filopodia were well isolated (no spines within 1 µm laterally and no spines above or below in *z*). To isolate NMDA-mediated EPSPs in Fig. 2, experiments were conducted as described for glutamate uncaging above, except stock MNI-caged glutamate solution (50 mM) was freshly diluted in Mg^{+2}-free aCSF to 10 mM and Mg^{+2}-free aCSF containing 20 µM DNXQ was washed on to the slice for at least 15 min.

Focal synaptic stimulation

Patch-clamp recordings were acquired in control aCSF. After whole-cell configuration, modified aCSF containing 120 mM NaCl, 3 mM KCl, 25 mM $NaHCO_3$, 1.25 mM NaH_2PO_4, 2 mM $CaCl_2$, 0 mM $MgCl_2$, 11 mM glucose, 3 mM sodium pyruvate, 1 mM ascorbic acid and 0.02 mM DNQX was washed on the slice for at least 15 min. Theta-glass bipolar stimulating electrodes filled with aCSF containing 0.05 mM Alexa Fluor 594 for visualization were positioned near dendritic filopodia (about 10 µm) under two-photon guidance. Stimuli were delivered with an AMPI Isoflex isolator. Stimulus intensity was increased until an action potential was initiated, and then intensity was decreased to generate EPSPs below the action potential threshold. Relative changes in fluorescence ($\Delta F/F$) of the Ca^{2+} indicator Fluo-4 were measured simultaneously at the tip of the filopodium and the parent branch. Trials in which synaptic stimulation resulted in somatic action potentials were excluded from further analysis. Only the trials with no detectable change in fluorescence of the parent branch were further analysed.

Plasticity experiments

For plasticity induction, two-photon glutamate uncaging at filopodia or spines of interest was followed in time (10 ms) by a backpropagating action potential, which was generated by injecting a 2-ms current pulse of 1.2–2 nA at the soma. This pairing was repeated 40 times at 2 Hz. Two control protocols were used at filopodia: pre alone (two-photon glutamate uncaging at filopodia was repeated 40 times at 2 Hz with no somatic action potentials) and post alone (without any caged glutamate present, two-photon laser pulses at filopodia were followed (10 ms) by a backpropagating action potential, repeated 40 times at 2 Hz). A longer spike-timing-dependent plasticity pairing protocol consisting of 90 repeats at 2 Hz was also used at spines (Extended Data Fig. 9).

For plasticity experiments in filopodia, a neighbouring spine was first stimulated separately with control pulses and the uncaging laser power was adjusted to yield large (0.2–1.2 mV) somatic EPSPs. Plasticity induction was applied using the same laser power. This was followed by test stimulations of filopodia using the same laser power about 3–5 min after the induction. Filopodia were excluded if they moved close (<0.1 µm) to other neighbouring spines owing to shape or size changes throughout the course of the experiment. The magnitude of plasticity was quantified as the average change in EPSP amplitude after the plasticity protocol. We did not calculate the percentage change to avoid division by small numbers (initial EPSP ≈ 0 mV). We chose to use the change in the protrusion length as a structural metric of the plasticity experiment because the estimation of spine volume is complicated by the increase of Alexa Fluor 488 fluorescence during the course of the experiment. Morphological and distance measurements were carried out using ImageJ/FIJI (National Institutes of Health) on two-dimensional images collected during the experiment.

For plasticity experiments in spines, a second spine on a different branch was used as a control and was not stimulated during plasticity induction. Both test and control spines were stimulated with test pulses before and after the plasticity protocol induction. Control filopodia were tested in separate cells from test filopodia. Spines and control filopodia were followed up to 20–30 min after the plasticity protocol induction. Care was taken not to move the uncaging location closer to the spine head during the experiment to avoid artificial increases in EPSP amplitudes. For the plasticity induction protocol with 90 repetitions, both test and control spines showed a slight decrease in EPSP amplitude, consistent with previous reports[45,46]. The magnitude of plasticity was quantified as the average change in EPSP amplitude after the plasticity protocol.

Reporting summary

Further information on research design is available in the Nature Portfolio Reporting Summary linked to this article.

Data availability

The data generated and analysed in the current study are available from the corresponding author upon reasonable request. Source data are provided with this paper.

Code availability

Code for image analysis can be accessed at https://github.com/harnett/FilopodiaStructuralSubstrateSilentSynapses.

41. Feng, G. et al. Imaging neuronal subsets in transgenic mice expressing multiple spectral variants of GFP. *Neuron* **28**, 41–51 (2000).
42. Yang, G., Chang, P. C., Bekker, A., Blanck, T. J. J. & Gan, W. B. Transient effects of anesthetics on dendritic spines and filopodia in the living mouse cortex. *Anesthesiology* **115**, 718–726 (2011).
43. Ji, N., Magee, J. C. & Betzig, E. High-speed, low-photodamage nonlinear imaging using passive pulse splitters. *Nat. Methods* **5**, 197–202 (2008).
44. Harnett, M. T., Xu, N. L., Magee, J. C. & Williams, S. R. Potassium channels control the interaction between active dendritic integration compartments in layer 5 cortical pyramidal neurons. *Neuron* **79**, 516–529 (2013).
45. Matsuzaki, M., Honkura, N., Ellis-Davies, G. C. R. & Kasai, H. Structural basis of long-term potentiation in single dendritic spines. *Nature* **255**, 243–244 (2004).
46. Weber, J. P. et al. Location-dependent synaptic plasticity rules by dendritic spine cooperativity. *Nat. Commun.* **7**, 11380 (2016).

Acknowledgements We thank D. H. Yun for technical assistance with eMAP, K. Tsimring and A. Krol for technical assistance with perfusions, and C. Yaeger, M. Tadross, E. Nedivi and M. Bear for constructive criticism of the manuscript. We thank H. Umemori for the donation of Thy1-GFP-M+ mouse pups. Financial support was provided by the Boehringer Ingelheim Fonds (D.V.), National Institutes of Health RO1NS106031 (M.T.H.), the James W. and Patricia T. Poitras Fund at MIT (M.T.H.), a Klingenstein-Simons Fellowship (M.T.H.), a Vallee Foundation Scholarship (M.T.H.) and a McKnight Scholarship (M.T.H.).

Author contributions D.V. performed all experiments, analysed all data and prepared the figures. K.C. provided eMAP resources. M.T.H supervised all aspects of the project and wrote the manuscript with D.V.

Competing interests The authors declare no competing interests.

Additional information
Supplementary information The online version contains supplementary material available at https://doi.org/10.1038/s41586-022-05483-6.
Correspondence and requests for materials should be addressed to Mark T. Harnett.
Peer review information *Nature* thanks Bernardo Sabatini and the other, anonymous, reviewer(s) for their contribution to the peer review of this work.
Reprints and permissions information is available at http://www.nature.com/reprints.

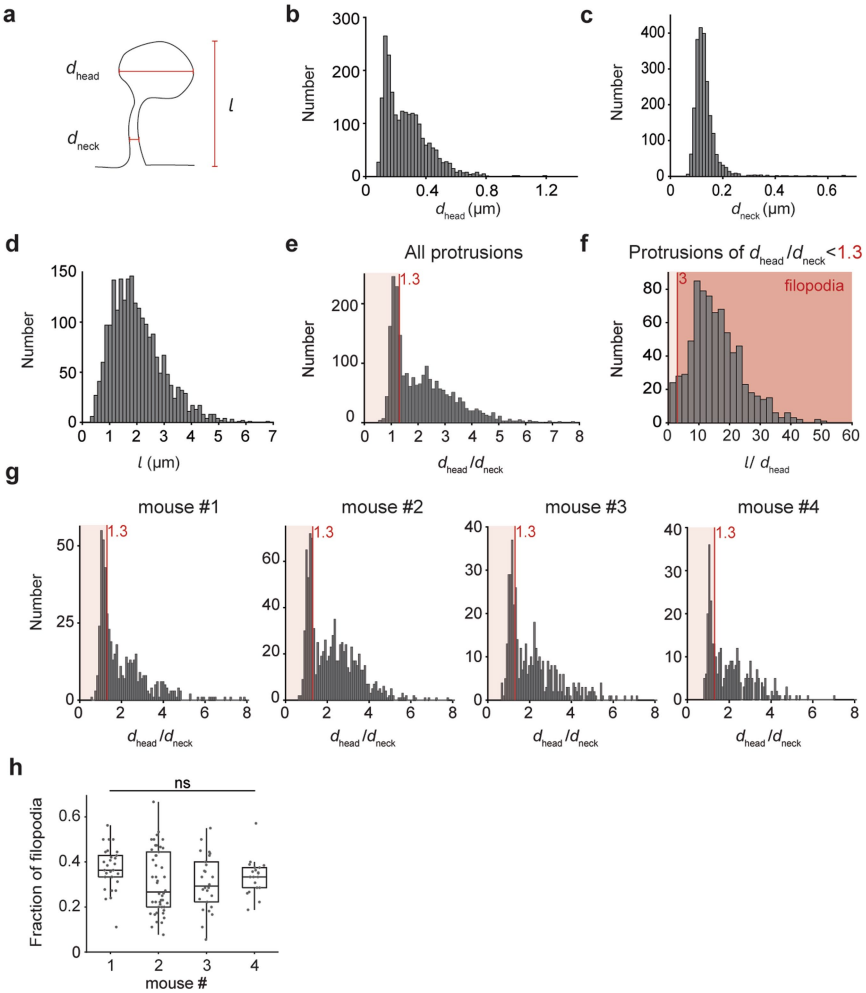

Extended Data Fig. 1 | Morphological measurements of dendritic protrusions. a, Illustration of a dendritic protrusion and corresponding measurements: head diameter. (d_{head}), neck diameter (d_{neck}), length (l). **b**–**d**, Population histograms of morphological characteristics across all dendritic protrusions (n = 2234). **e**, Population histogram of the relationship between d_{head} and d_{neck}. Shaded area indicates a ratio below 1.3, the first criterion used to classify filopodia versus spines. **f**, Population histogram of d_{head}/l for protrusions with d_{head}/d_{neck} below 1.3 (shaded area in **e**). Protrusions with d_{head}/l above 3 were classified as filopodia, those below 3 were likely short stubby spines and were not analyzed further (shaded area= (d_{head}/d_{neck} < 1.3) ∩ (l/d_{head}>3)). **g**, Same as **e** but for each of the 4 mice. **h**, Fraction of dendritic protrusions classified as filopodia per mouse (n = 527, 944, 435, 328 dendritic protrusions and 30, 47, 25, 21 dendritic branches for mouse 1, 2, 3, 4 respectively). Box plot represents median and IQR with whiskers extending to the most extreme points not considered outliers. ns P = 0.093, Kruskal-Wallis test.

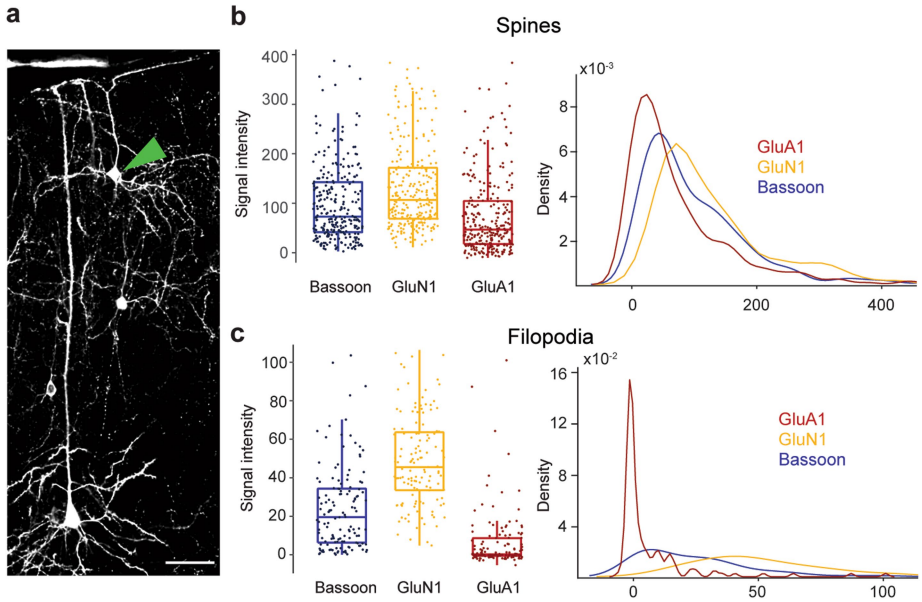

Extended Data Fig. 2 | Filopodia in L2/3 pyramidal neurons exhibit AMPAR immune-negative and NMDAR immune-positive synapses. a, Example confocal image of a V1 L2/3 neuron (green arrowhead) expressing GFP after viral transfection in V1 in an originally 45 µm thick slice. Scale bar: 100 µm expanded/ 59 µm original. Image was taken after reshrinking the tissue from 4x expansion to 1.7x expansion. **b**, Box plot (left) and kernel density estimate (right) of signal intensity in Bassoon (blue), NMDAR (yellow), and AMPAR (red) channels for L2/3 pyramidal neuron spines ($n = 275$). Box plot represents median and IQR with whiskers extending to the most extreme points not considered outliers. Signal in each channel is shown for all dendritic protrusions, each represented by one dot. **c**, As in b, but for filopodia ($n = 134$).

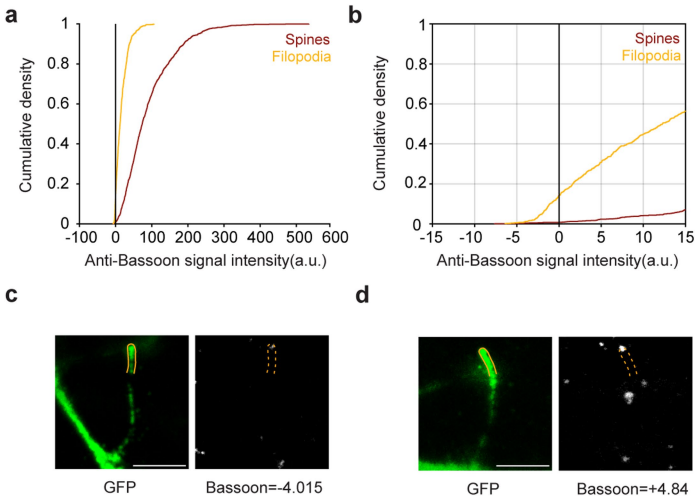

Extended Data Fig. 3 | Anti-Bassoon signal intensity threshold for presence of presynaptic partner. a, Cumulative density function of Bassoon signal intensity in spines (red) and filopodia (yellow). Vertical line at the choosen threshold (anti-Bassoon signal = 0). **b**, Magnified plot of **a** around 0. **c**-**d**, Example filopodia with anti-Bassoon signal intensities below above the threshold. Scale bar: 5 µm expanded/1.25 µm original.

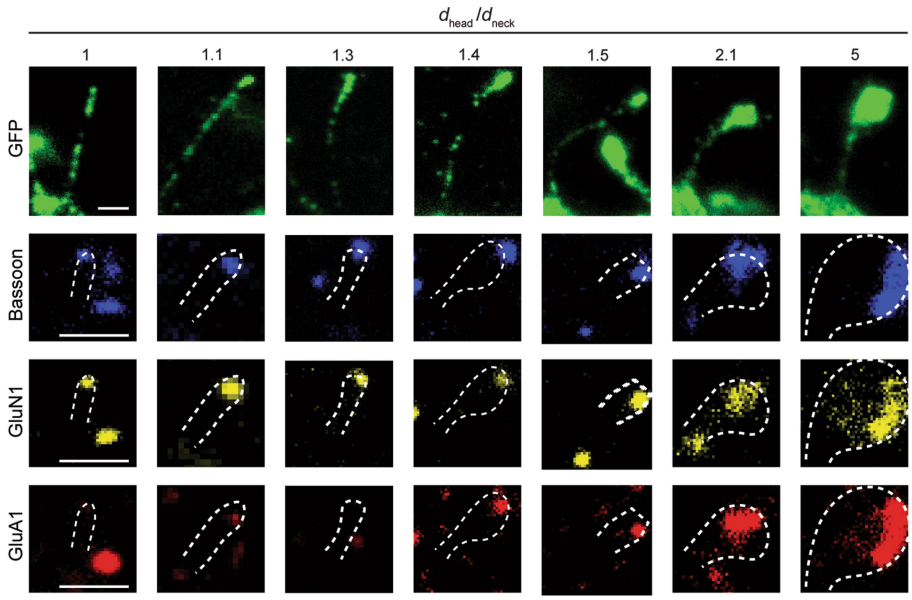

Extended Data Fig. 4 | Representatitive examples of eMAP at dendritic protrusions. Example four channel images of dendritic protrusions with different d_{head}/d_{neck} values (increasing from left to right). From top to bottom: cell-filling GFP stained with Alexa Fluor 488 (green) at lower magnification to show full protrusion shape, presynaptic protein Bassoon stained Alexa Fluor 405 (blue), NMDAR subunit NR1(GluN1) stained with Alexa Fluor 555 (yellow), and AMPAR subunit GluR1(GluA1) stained with Alexa Fluor 647 (red), all at higher magnifiaction to show synaptic localization. Scale bar: 2 µm expanded/0.5 µm original.

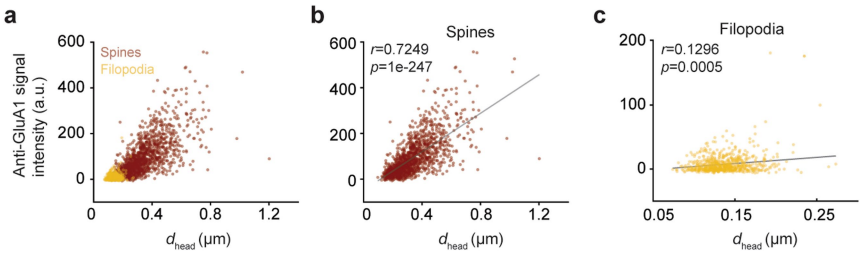

Extended Data Fig. 5 | Anti-GluA1 signal increases with spine size. a, Anti-GluA1 signal intensity as a function of head diameter for spines (red) and filopodia (yellow). **b**, Correlation between head diameter and anti-GluA1 signal intensity for spines. The data are fitted with a line of slope 421+/−22 using linear regression. **c**, Correlation between diameter of filopodium head and anti-GluaA1 signal intensity. The data are fitted with a line of slope 95+/−39 using linear regression. Correlation coefficients (*r*) and *p*-values were obtained from a two-tailed, non-parametric Spearman correlation.

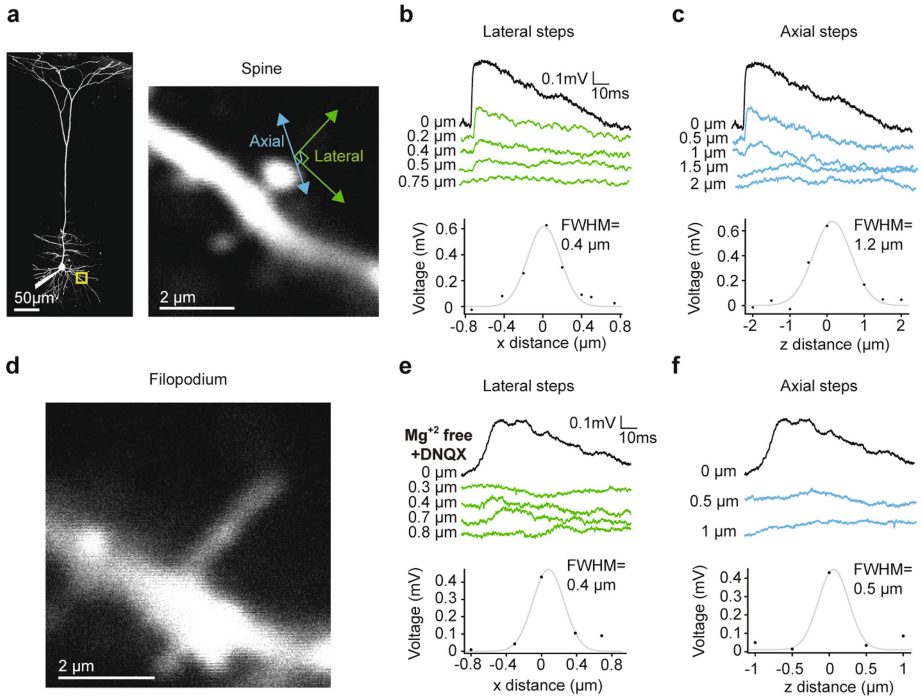

Extended Data Fig. 6 | Spatial resolution of two-photon MNI-glutamate uncaging at adult mouse cortical protrusions. a, Left: Two-photon z-stack of a V1 L5 pyramidal neuron filled with Alexa-488 via somatic patch pipette. Basal branch segment of interest indicated by yellow box. Right: Magnified view of basal branch of interest. **b**, (top) Voltage response for the spine at lateral uncaging locations shown in **a.** (bottom) plot of lateral uncaging resolution. Continuous line is the Gaussian fit of the amplitudes of two-photon glutamate uncaging along lateral steps (circles). **c**, (top) Voltage response for the spine at axial locations shown in **a**. Each voltage trace is an average of the voltage traces evoked at a specific axial step above and below of the spine. (bottom) plot of axial uncaging resolution (see **b**). **d**, Magnified view of a filopodium of a basal branch of a L5 pyramidal neuron. All uncaging experiments shown in **e** and **f** were performed in Mg^{2+} free ASCF with AMPA blocked (DNQX, 20 µM). **e**, As in **b**, for the filopodium shown in **d**. **f**, As in **c**, for the filopodium shown in **d**.

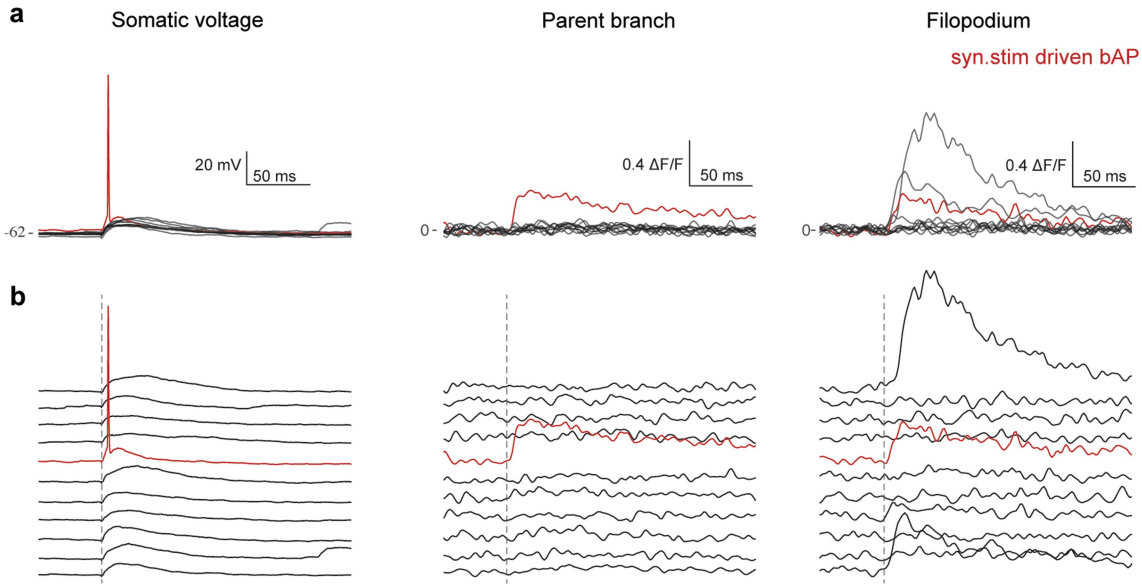

Extended Data Fig. 7 | Responses to focal extracellular synaptic stimulation for the filopodium shown in Fig. 3e. a, Superimposed traces of somatic voltage recordings (left) and corresponding changes in local Ca^{2+} (measured via Fluo-4 fluorescence; ΔF/F) at the parent dendritic branch (middle) and at the tip of the filopodium (right) in response to focal extracellular synaptic stimulation in Mg^{2+}-free aCSF with AMPA blocked (via DNQX, 20 µM). All synaptic stimulation successes and failures for the filopodium in Fig. 3e are shown. Synaptic stimulation driven backpropagating action potential (bAP) shown in red. **b**, Same as in **a** with traces spaced apart. Grey dashed line indicates the onset of synaptic stimulation.

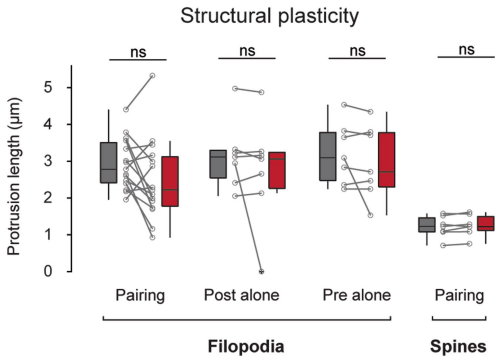

Extended Data Fig. 8 | Length of protrusions before and after induction protocols. Length of protrusions before (grey) and after (red) induction in filopodia and spines. Three different induction protocols were tested in filopodia: i- Pairing protocol (n = 15 filopodia from 13 slices and 10 mice); ii- Somatic action potentials without any caged glutamate present (Post alone; n = 7 filopodia from 7 slices and 6 mice); iii- Glutamate uncaging without somatic action potential (Pre alone; n = 7 filopodia from 7 slices and 6 mice); ns $P > 0.15$. Two-sided Wilcoxon signed-rank test. Box plot represents median and IQR with whiskers extending to the most extreme points not considered outliers.

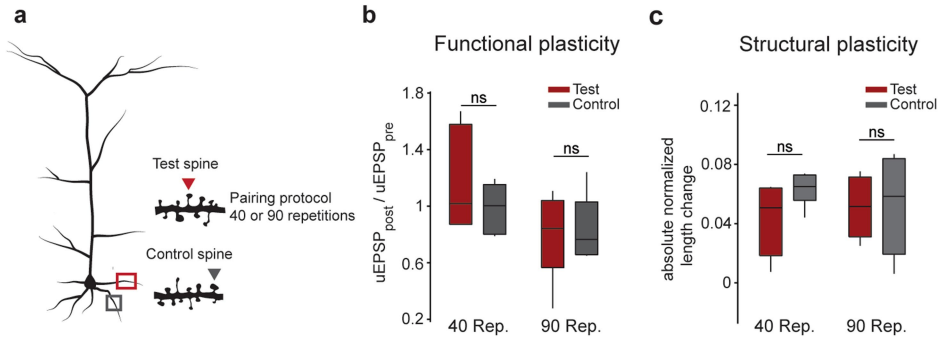

Extended Data Fig. 9 | Spiny synapses do not exhibit changes in synaptic strength or length in response to the STDP protocol. a, Schematic of the experiment. A control spine on a different branch than the branch of the test spine was always present. 40 and 90 repetitions of the pairing protocol were used for spines. **b**, Relative change of peak somatic uEPSP amplitude after pairing. P = 0.5781 (40 repetitions, $n = 7$ test and 7 control spines from 7 slices and 4 mice), $P = 0.9375$ (90 repetitions, $n = 7$ test and 7 control spines from 7 slices and 3 mice), two-sided Wilcoxon signed-rank test. Box plot represents median and IQR with whiskers extending to the 95% CI. **c**, Relative change of spine length after pairing. $P = 0.4688$ (40 repetitions, $n = 7$ test and 7 control spines from 7 slices and 4 mice), $P = 0.8125$ (90 repetitions, $n = 7$ test and 7 control spines from 7 slices and 3 mice), two-sided Wilcoxon signed-rank test. Box plot represents median and IQR with whiskers extending to the 95% CI.

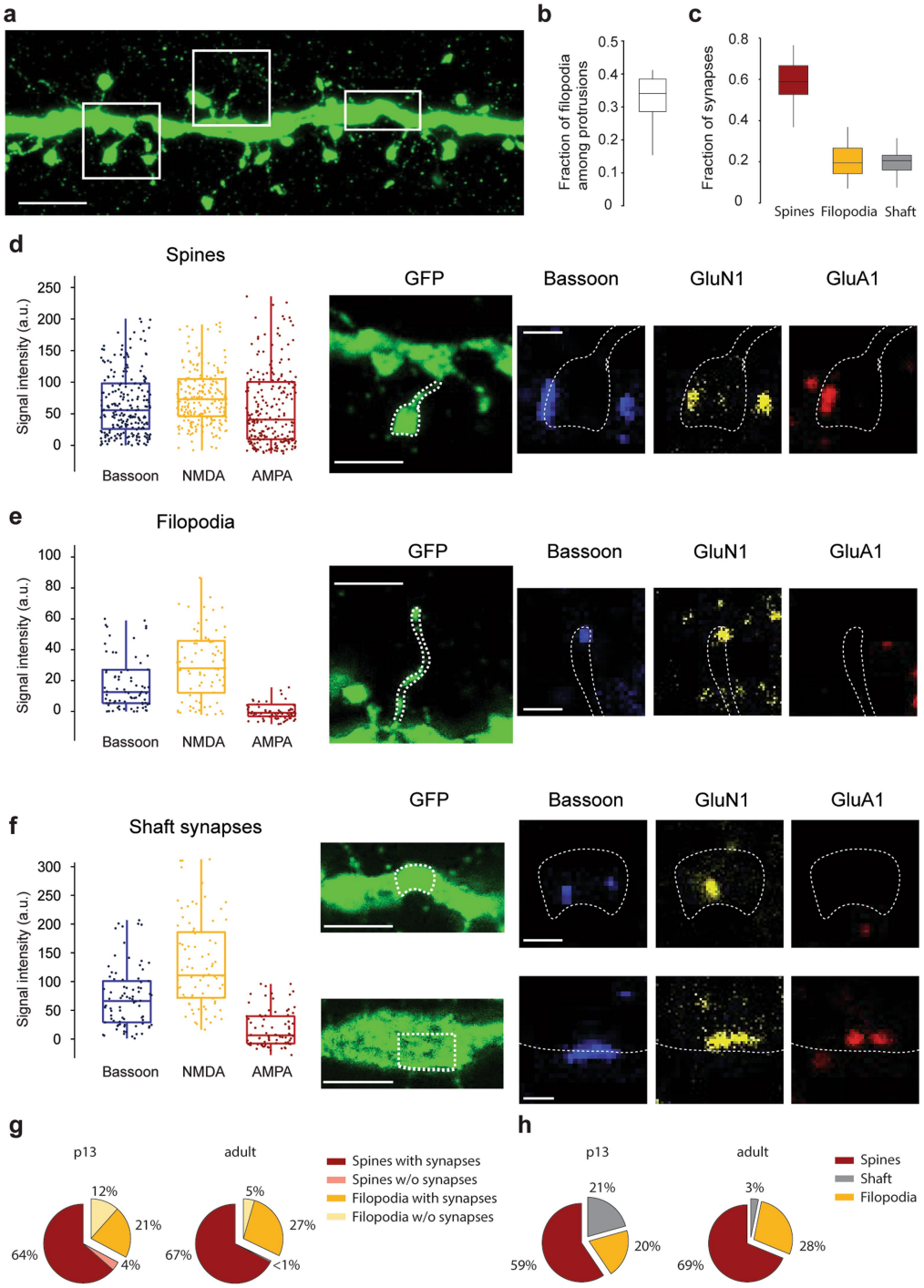

Extended Data Fig.10 | Super-resolution characterization of synapses in developing mouse visual cortex. a, Example confocal image of a postnatal day (P) 13 Thy1- GFP-M+ L5 pyramidal neuron dendritic segment after 4x expansion. Scale bar: 10 µm expanded/2.5 µm original. **b**, Fraction of dendritic protrusions classified as filopodia in P13 L5 PNs (n = 371 dendritic protrusion, 18 dendritic branches, 3 mice). Box plot represents median and IQR with whiskers extending to the most extreme points not considered outliers. **c**, Fraction of total synapses in the three dendritic locations in P13 L5 PNs (n = 397 synapses, 18 dendritic branches, 3 mice). Box plot represents median and IQR with whiskers extending to the most extreme points not considered outliers. **d**, (left) Box plot and individual data for signal intensity in Bassoon (blue), NMDAR (yellow), and AMPAR (red) channels for spines (n = 236). (right) example four channel images of a representative spine. Box plot represents median and IQR with whiskers extending to the most extreme points not considered outliers. Scale bar: 5 µm expanded/1.25 µm original (GFP), 1 µm expanded/0.25 µm original (Bassoon). **e**, As in **b**, but for filopodia (n = 79). **f**, As in **b**, but for shaft synapses (n = 82). Example images show a shaft synapse that lacks AMPARs (top) and a shaft synapse that exhibits AMPARs (bottom). **g**, Comparison of dendritic protrusion types in P13 (n = 371) and adult mice (n = 2234). **h**, Comparison of synapse distribution in P13 (n = 397) and adult mice (n = 2188).

nature portfolio

Corresponding author(s): Mark Harnett

Last updated by author(s): Sep 30, 2022

Reporting Summary

Nature Portfolio wishes to improve the reproducibility of the work that we publish. This form provides structure for consistency and transparency in reporting. For further information on Nature Portfolio policies, see our Editorial Policies and the Editorial Policy Checklist.

Statistics

For all statistical analyses, confirm that the following items are present in the figure legend, table legend, main text, or Methods section.

n/a	Confirmed
☐	☒ The exact sample size (*n*) for each experimental group/condition, given as a discrete number and unit of measurement
☐	☒ A statement on whether measurements were taken from distinct samples or whether the same sample was measured repeatedly
☐	☒ The statistical test(s) used AND whether they are one- or two-sided *Only common tests should be described solely by name; describe more complex techniques in the Methods section.*
☐	☒ A description of all covariates tested
☐	☒ A description of any assumptions or corrections, such as tests of normality and adjustment for multiple comparisons
☐	☒ A full description of the statistical parameters including central tendency (e.g. means) or other basic estimates (e.g. regression coefficient) AND variation (e.g. standard deviation) or associated estimates of uncertainty (e.g. confidence intervals)
☐	☒ For null hypothesis testing, the test statistic (e.g. *F*, *t*, *r*) with confidence intervals, effect sizes, degrees of freedom and *P* value noted *Give P values as exact values whenever suitable.*
☒	☐ For Bayesian analysis, information on the choice of priors and Markov chain Monte Carlo settings
☒	☐ For hierarchical and complex designs, identification of the appropriate level for tests and full reporting of outcomes
☐	☒ Estimates of effect sizes (e.g. Cohen's *d*, Pearson's *r*), indicating how they were calculated

Our web collection on statistics for biologists contains articles on many of the points above.

Software and code

Policy information about availability of computer code

Data collection	Leica Application Suite X (LAS X), Bruker Prairie View Software 5.4
Data analysis	ImageJ Version 2.1.0/1.53c, Mathworks MATLAB_r2020b

For manuscripts utilizing custom algorithms or software that are central to the research but not yet described in published literature, software must be made available to editors and reviewers. We strongly encourage code deposition in a community repository (e.g. GitHub). See the Nature Portfolio guidelines for submitting code & software for further information.

Data

Policy information about availability of data

All manuscripts must include a data availability statement. This statement should provide the following information, where applicable:

- Accession codes, unique identifiers, or web links for publicly available datasets
- A description of any restrictions on data availability
- For clinical datasets or third party data, please ensure that the statement adheres to our policy

The data generated and analyzed in the current study are available from the corresponding authors upon reasonable request. Source data are provided with this paper.

Field-specific reporting

Please select the one below that is the best fit for your research. If you are not sure, read the appropriate sections before making your selection.

☒ Life sciences ☐ Behavioural & social sciences ☐ Ecological, evolutionary & environmental sciences

For a reference copy of the document with all sections, see nature.com/documents/nr-reporting-summary-flat.pdf

Life sciences study design

All studies must disclose on these points even when the disclosure is negative.

Sample size	Sample size was not predetermined. Sample sizes are comparable or larger to similar studies (Sun, C. et al. (2021) 'The prevalence and specificity of local protein synthesis during neuronal synaptic plasticity', Science Advances, 7(38), pp. 1–14. doi: 10.1126/sciadv.abj0790. Araya, R., Vogels, T. P. and Yuste, R. (2014) 'Activity-dependent dendritic spine neck changes are correlated with synaptic strength', Proceedings of the National Academy of Sciences of the United States of America, 111(28). doi: 10.1073/pnas.1321869111.). For Magnified Analysis of the Proteome (MAP), more than 3000 protrusions were imaged, taken from 10 animals, and for electrophysiology, between 5 and 15 cells per experiment were included.
Data exclusions	Magnified Analysis of the Proteome (MAP): all dendritic branches that contained signal in the GFP, Bassoon, GluA1 and GluN1 were analyzed and included. Two photon imaging and uncaging: Cells without healthy responses to current injection were not included. Experiments were terminated if signs of photodamage were detected (increase in basal fluorescence, loss of transient signals and/or depolarization).
Replication	Findings were not replicated due to the study design. Analyses were conducted independently across different mice (Extended Data Fig. 1). The study consists of >2000 anatomical measurements, >3000 protein expression measurements, and >200 physiological measurements across multiple distinct categories in different mice.
Randomization	No randomization was used due to study design, aside from sex, which was balanced.
Blinding	Structural measurements in the GFP channel were all performed blind with respect to the Bassoon, AMPAR and NMDAR channels. There was no blinding for other experiments as there was no sample allocation.

Reporting for specific materials, systems and methods

We require information from authors about some types of materials, experimental systems and methods used in many studies. Here, indicate whether each material, system or method listed is relevant to your study. If you are not sure if a list item applies to your research, read the appropriate section before selecting a response.

Materials & experimental systems

n/a	Involved in the study
☐	☒ Antibodies
☒	☐ Eukaryotic cell lines
☒	☐ Palaeontology and archaeology
☐	☒ Animals and other organisms
☒	☐ Human research participants
☒	☐ Clinical data
☒	☐ Dual use research of concern

Methods

n/a	Involved in the study
☒	☐ ChIP-seq
☒	☐ Flow cytometry
☒	☐ MRI-based neuroimaging

Antibodies

Antibodies used	The following primary antibodies were used: Anti-GFP (ThermoFisher Scientific A10262), Anti-NMDAR1 (SYSY 114011), Anti-AMPAR1 (SYSY 182003), Anti-Bassoon (SYSY 141004) The following secondary antibodies were used:: Goat Anti-Guinea pig IgG H&L (Alexa Fluor® 405) (Abcam ab175678), Goat anti-Mouse IgG (H+L) Highly Cross-Adsorbed Secondary Antibody, Alexa Fluor Plus 555 (ThermoFisher Scientific A32727), Goat anti-Rabbit IgG (H+L) Highly Cross-Adsorbed Secondary Antibody, Alexa Fluor Plus 647 (ThermoFisher Scientific A32733), Goat anti-Chicken IgY (H+L) Secondary Antibody, Alexa Fluor 488 (ThermoFisher Scientific A-11039). Dilution 1:20 for primary and 1:10 for secondary antibodies.
Validation	The validation for Anti-GFP (ThermoFisher Scientific A10262) can be found here: https://www.thermofisher.com/antibody/product/GFP-Antibody-Polyclonal/A10262 The validation for Anti-NMDAR1 (SYSY 114011) can be found here: https://sysy.com/product/114011 The validation for Anti-AMPAR1 (SYSY 182003) can be found here: https://sysy.com/product/182003 The validation for Anti-Bassoon (SYSY 141004) can be found here: https://sysy.com/product/141004

Animals and other organisms

Policy information about studies involving animals; ARRIVE guidelines recommended for reporting animal research

Laboratory animals	The following mouse lines were used: C57BL/6 mice (obtained from Charles River Laboratories), Thy1-GFP-M mice (obtained from Jackson Laboratory stock no.007788). Male and female mice were used in approximately equal numbers at 8-10 weeks of age or at postnatal day 13.
Wild animals	This study did not involve wild animals.
Field-collected samples	This study did not involve field-collected samples
Ethics oversight	NIH, Massachusetts Institute of Technology Committee on Animal care guidelines

Note that full information on the approval of the study protocol must also be provided in the manuscript.